Genetic and developmental constraints drive parallelism in flower evolution

Kevin Sartori[a,1], Natalia Wozniak[b,1], Anahid Powell[b,1], Ushio Fujikura[b], Christian Kappel[b], Tian-Feng Lü[c,d], Yang Dong[c,d], Stefanie Rosa[a], Michael Lenhard[b] and Adrien Sicard[a*]

[a] Uppsala Biocenter, Department of Plant Biology, BOX 7080, 750 07, Uppsala, Sweden Institut für

[b] Biochemie und Biologie, Universität Potsdam, Karl-Liebknecht-Str. 24-25, 14476 Potsdam-Golm, Germany

[c] State Key Laboratory of Plant Diversity and Specialty Crops, Institute of Botany, Chinese Academy of Sciences, 20 Nanxincun, Xiangshan, Beijing 100093, China

[d] China National Botanical Garden, Beijing 100093, China

[1] These authors contributed equally

* Corresponding author: Adrien Sicard (adrien.sicard@slu.se)

Abstract

Evolution repeatedly gives rise to similar phenotypes, reflecting shared constraints across independent lineages. In flowering plants, transitions to self-fertilization are typically accompanied by reduced flower size, but the mechanisms behind this pattern remain unclear. We show that two independently evolved self-fertilizing species of *Capsella* both achieved petal reduction by reducing the activity of the growth-promoting gene *JAGGED*. Because petal development is especially sensitive to JAGGED dosage, modest reductions limit petal growth with minimal effects on other organs, thus minimizing pleiotropy. Both species relied, at least partly, on the same ancestral genetic variants, revealing that preexisting diversity maintained in the ancestral population also facilitated this convergence. These findings illustrate how development constraints and ancestry can channel evolution toward predictable outcomes.

Evolution often produces similar traits across unrelated lineages, suggesting that outcomes are shaped by predictable constraints rather than chance. Such convergent phenotypes often arise in species exposed to similar ecological pressures, implying that adaptive solutions are limited (*1*). Beyond ecology, developmental constraints within Gene Regulatory Networks (GRNs) also restrict the range of viable phenotypes (*2*, *3*). Because GRNs carry historical legacies, closely related species often share the same constraints and thus respond similarly to shifts in selection pressures (*4*). Although specific cases of genetic convergence have been identified, the general mechanisms that drive repeated phenotypic evolution remain poorly understood (*5*).

Cross-pollination is common in plants and often enforced by self-incompatibility systems, which make reproduction dependent on animal pollinators (*6–10*). To attract pollinators, plants invest in large floral displays (*11–13*). Yet self-incompatibility has repeatedly broken down throughout evolution, producing self-fertilizing (selfing) lineages, likely as reproductive assurance when mates are scarce (*14*). Remarkably, independent transitions to selfing often converge on similar floral changes, collectively termed the selfing syndrome, with a hallmark being a pronounced reduction in flower and petal size (*6*, *14*). Genetic studies indicate that floral traits often evolve independently of one another or of vegetative traits, suggesting adaptive changes targeting specific organ dimensions (*15–23*). Yet because most growth regulators in plants are pleiotropic, influencing multiple organs (*24*), such specific changes likely depend on rare organ-specific regulators or on regulatory elements within pleiotropic genes. It remains, nevertheless, unclear which general growth regulators can be modulated at an organ-specific level and how such targeted changes in organ size occur. If such a regulation is limited, it could help explain phenotypic convergence following transitions to selfing. Beyond pleiotropy, the effect size and availability of adaptive variation in ancestral populations may further constrain evolution (*25*).

In this study, we exploit the *Capsella* genus as a model to study the convergent evolution of flowers after independent transitions to selfing (*26–33*). In this genus, the selfing species *C. rubella* (*Cr*) and *C. orientalis* (*Co*) evolved independently from an outcrossing *C. grandiflora* (*Cg*)-like ancestor following the breakdown of self-incompatibility, diverging ~100 kya and within the last 2 million years, respectively (**Fig. 1A**) (*28*, *34–36*). Both exhibit a fully established selfing syndrome, including a pronounced reduction in petal size (**Fig. 1)** (*37*).

61 **Convergent petal size reduction via similar reduction of distal cell proliferation**

62 A major phenotypic change in *Cr* and *Co* is a pronounced reduction in petal size, accompanied
63 by fewer cells, implicating altered cell proliferation as a central mechanism (*38*). To examine
64 the developmental basis of these changes, we analyzed cellular patterns along the proximal-
65 distal axis of petals, incorporating various descriptors of cell shape and directional growth
66 (**Table S1**). Petals exhibit two distinct cell clusters. A proximal cluster of large, elongated cells
67 and a distal cluster of small, rounded cells, separated by a transition zone where cell size and
68 anisotropy gradually decrease (**Fig. 1B and S1**). While this pattern is largely conserved across
69 species, cellular features along this axis can distinguish the petals of selfers from those of the
70 outcrosser (one-way ANOVA: $F(1,13) = 28.54$, $p = 0.00013$, $\eta^2 = 0.687$) (**Fig. 1B, 1D, S1, and**
71 **S2**). Selfers differ primarily in the distal region, where cell number is reduced roughly five-fold
72 compared to the outcrosser, resulting in a two-fold reduction in length and a three-fold decrease
73 in width (**Fig. 1E and S1C; Table S2**). Early petal growth occurs via cell proliferation, which
74 initially takes place throughout the primordia. Once the petal primordia reach approximately 90
75 µm in length, proliferation rapidly becomes restricted to the distal region, thereby determining
76 the size of the distal section, while cell elongation is largely confined to the proximal domain
77 (**Fig. 1 and S3**). In selfers, cell proliferation in the distal margin, as judged from the number of
78 S-phase cells, is reduced three- to four-fold relative to the outcrosser, consistently across both
79 lineages (**Fig. 1F and 1G**). Thus, despite independent origins, petal size reduction in these
80 selfing species arises through the same developmental mechanism: restricted growth at the
81 distal margin due to decreased cell division.

82 **Independent selfing lineages co-opted *JAG* to reduce petal size**

83 The convergence in petal development suggests that similar genetic mechanisms underlie size
84 reduction in the two selfing species. Previous studies indicated that half of the loci associated
85 with petal size are shared between *Cr* and *Co*, with PAQTL2 on chromosome 2 contributing
86 most to phenotypic evolution (**Fig. S4 A**) (*38*, *39*). To refine the location of PAQTL2 in each
87 selfing species, we introgressed the outcrossing *Cg* alleles into each selfer, creating near-
88 isogenic lines (*NILrg1* and *NILog2*) and screened for recombinants with this region (**Fig. 2**).
89 By analyzing petal size segregation in the progeny, we narrowed down the causal mutation (s)
90 to 14.6 kb in *Cr* and 130 kb in *Co*. The most informative recombinants from *NILrg1* indicated
91 that the causal mutation(s) are situated between 9,061,779 and 9,076,392 bp on chromosome 2.
92 We confirmed this region by generating a quasi-isogenic line (*qILrg*) for the 14.6-kb interval,

where *Cr* homozygotes exhibited ~20% smaller petals than *Cg* homozygotes, recapitulating the PAQTL2 effect (**Fig. S4C and S7A**). In *NILog2*, the most informative recombinant localized the causal mutation to 9,019,066–9,149,619 bp on chromosome 2, accounting for a 25% petal reduction in *Co* (**Fig. 2B and S7A**). This region overlaps with the locus identified in *Cr*, confirming that the same genomic locus underpins PAQTL2 in both selfing species.

The 14.6-kb interval contained only two genes, including the *Arabidopsis thaliana JAGGED* (*JAG*) ortholog, a zinc-finger transcription factor, known to control lateral organ growth and distal cell proliferation (**Fig. 2A**) (*40*). In an EMS-mutagenized *C. rubella* screen, we identified a mutant phenocopying the *A. thaliana jag* mutation (**Fig. S6A**)(*40*). Bulked-segregant analysis revealed a splice-site mutation in the third exon of *JAG*, preventing proper splicing and introducing a premature stop codon (**Fig. S5**). The defect was rescued by reintroducing a wild-type *Cr* allele, confirming *JAG* inactivation as causal (**Fig. S6B**). We thus used this mutant in a quantitative complementation test (*41*) to test whether *JAG* underlies PAQTL2 in both selfers. In this assay, natural alleles were crossed to a jag+/– background, where functional differences between the natural alleles are expected to be amplified only when the loss-of-function mutation affects the same gene. Consistently, in both cases, the differences between the selfer and outcrosser alleles were stronger when combined with the mutant alleles (**Fig. 2C and D**). Linear model analysis revealed a significant interaction between the tested (*Cg1* and *Cr* or *Cg2* and *Co*) and control allele (WT and *crjag*) (β = -0.38976 ± 0.08710, t = -4.475, $p = 8.56 \times 10^{-6}$ for *NILog*; and β = 0.311 ± 0.043, t = 7.245, $p = 2.27 \times 10^{-12}$ for *qILrg*), indicating that polymorphism within *JAG* contributed to a reduction in petal size in both cases. To further confirm *JAG's* role, we transformed genomic constructs corresponding to the *Cg* (*JAGg1*) and *Cr* (*JAGr*) alleles segregating in *NILrg*, as well as the *Cg* (*JAGg2*) and *Co* (*JAGo*) alleles from *NILog*, into the *A. thaliana jag-2* mutant (**Fig. S4D and E**). All alleles rescued the mutant phenotype, but *Cg1* and *Cg2* alleles produced larger petals than *Cr* and *Co* alleles, respectively. These results further support that allelic variation in *JAG* underlies convergent petal size reduction in both selfing species.

***JAG* is essential to promote distal petal cell proliferation**

Inactivation of *JAG* in *Cr* causes pleiotropic effects, leading to a ≥10% reduction in the size of most organs, with particularly strong effects on leaves (30%), petals (60%) (**Fig. S6**), and fruit. To uncover the developmental basis, we compared wild-type and *crjag* petals. Silhouette overlays showed that the proximal petal region was largely unaffected, whereas the distal region

125 was almost entirely missing (**Fig. 3A and 3B**). Cellular analysis revealed a ~5-fold reduction
126 in total cell number (**Fig. 3C and 3D**). This reduction in cell number was particularly
127 pronounced in the transition and distal zones (**Fig. 3D**). Cell elongation in the proximal region
128 and the position of the transition zone were largely unaffected, indicating that overall petal
129 growth patterning is not altered by *JAG* (**Fig. 3B**). However, growth in the marginal part of the
130 petal was almost completely abolished, with only a few small rounded cells formed within the
131 distal area. This was associated with more than a twofold reduction in the number of cell
132 proliferation events at the onset of cell proliferation within the distal part of the petal primordia
133 (**Fig. 3E and F**). Together, these results indicate that *JAG* is essential for promoting and
134 maintaining a high rate of cell proliferation at the petal margin. Lack of function almost
135 completely abolishes growth in the distal region. These observations suggest that *JAG* does not
136 affect the overall growth pattern of the petal but instead promotes cell proliferation within the
137 distal margin, providing strong support for its proposed function as a distal growth promoter
138 during petal development (*42*) and explaining the cellular basis of convergent petal size
139 reductions in *Capsella* (**Fig. 1**).

140 **Cis-regulatory changes in *JAG* drive petal size reduction in selfing *Capsella* species**

141 To assess the impact of allelic variation at *JAG*, we compared petal morphology in the *NILog*
142 and *qILrg* lines (**Fig. 4 A-D**). Consistent with the loss of *JAG* function, both showed a selective
143 reduction in distal petal growth, with total petal area decreased by 22% and 15%, respectively
144 (**Fig. S7**). This reduction reflected a lower total cell number, most pronounced at the distal tip.
145 Strikingly, the effect was specific to petals; other floral organs and leaves were unaffected, in
146 contrast to the broad reductions seen in *crjag*. These results suggest that *JAG* activity has been
147 selectively modified during petal development.

148 Among the polymorphisms distinguishing the tested *JAG* alleles, four resulted in amino acid
149 substitutions, but none affected conserved regions or the C2H2 zinc-finger domain.
150 Furthermore, promoter-swap experiments revealed a cis-regulatory basis. *A. thaliana jag-2*
151 mutants transformed with the *Cr* coding sequence under the *Cg1* promoter (*pJAGg1::JAGr*)
152 developed significantly larger petals than those carrying the reciprocal construct
153 (*pJAGr::JAGg1*) (Fig. S4 D). Moreover, *jag-2*; *pJAGr::JAGg1* petals were similar in size to
154 *jag-2*; *JAGr* petals and significantly smaller than *jag-2*; *JAGg1* petals (**Fig. S4**). Thus, in *Cr*,
155 differences in *JAG* activity are explained by cis-regulatory rather than protein-coding changes.

Because both selfers share the same non-synonymous substitutions, these are unlikely to contribute in *Co* also suggesting cis-regulatory evolution in this species.

Subtle changes in *JAG* dosage drive petal size evolution with minimal pleiotropy

Single-cell analysis revealed reduced *JAG* expression in developing petals, sepals, and the inflorescence meristem –of the selfers compared to the outcrosser (**Fig. S8**). Because *JAG* promotes cell division (*43*), its reduced activity likely explains -the lower -proliferation observed at the petal margin. Yet, only petals showed strong size reduction, suggesting heightened sensitivity to *JAG* dosage. This is consistent with the severe petal defects of *jag* mutants and the established role of *JAG* in driving distal petal growth.

To test whether *JAG* dosage could explain petal size differences, we used an existing petal growth model based on the Growing Polarized Tissue (GPT) framework (*44*) (**Fig. S9**). In this model, tissue polarity is generated by diffusion of a polariser (POL) produced by the basal organiser (PROXORG), which drives growth along the proximal-distal axis (Kpar). The distal factors (DGRAD, DISTORG) promote lateral (Kper) and divergent growth from the petal midline, respectively. The model reproduces *A. thaliana* petals and is consistent with *JAG* functioning as DGRAD, with the phytohormone auxin signalling contributing to the polarity field establishment (*44*). However, it failed to capture *Capsella* petal shapes (**Fig. S9**). Adjusting the model by broadening DGRAD and DISTORG domains and allowing DGRAD to also influence Kpar yielded realistic *Cg* petals (**Fig. 4, S9 and Supplementary Materials**). With this new model, the complete loss of DGRAD, combined with fragmented auxin distribution (as in (*44*)), produced short and narrow 'jagged' petals phenocopying the *crjag* mutants. Quantitative tuning showed that even modest reductions in *JAG* activity had strong effects on petal size. A 10% decrease in its effects on Kper and Kpar led to a 23% reduction in petal size, while a 25% reduction in *JAG* resulted in more than a twofold decrease in petal size (**Fig. 4E)**.

To test whether organ-specific sensitivity could explain the minimal pleiotropy of change in *JAG* expression, we next used an existing leaf growth model (*45*) (**Fig. S10**). In this framework, a PGRAD gradient along the proximal-distal axis regulates growth parallel to the axis (Kpar), while the broadly expressed factor LAM promotes perpendicular growth (Kper), which is further inhibited by MID along the central axis. At later stages, LATE reduces Kpar and enhances Kper activation by LAM. Because *crjag* leaves show a 14% reduction in length and 18% in width, we hypothesised that *JAG* contributes to both PGRAD and LAM activity,

188 consistent with its expression at proximal side of leaf and sepal margins (*40*, *46*, *47*). Calibrating
189 the model to match the *crjag* phenotype and running both the petal and leaf models for a similar
190 number of iterations under different *JAG* dosage revealed that petals were far more sensitive to
191 *JAG* reduction. At 75% activity, petal area had already decreased by ~30%, whereas leaf area
192 was reduced by less than 15%, and this contrast becomes even stronger at lower dosage levels
193 (**Fig. S10**).

194 This analysis shows that modest decreases in *JAG* activity strongly affect petal growth but have
195 only minor effects on other organs. Such heightened sensitivity may represent a developmental
196 constraint and helps explain why *JAG* has been repeatedly co-opted to reduce petal size in
197 different lineages. Because *JAG* plays a central role in promoting petal growth while
198 contributing less to other organs, even subtle changes in its activity can drive major
199 evolutionary shifts in petal morphology with minimal pleiotropic consequences.

200 **Standing variation facilitates parallel petal size evolution**

201 A notable observation was that polymorphisms affecting *JAG* function in both selfing lineages
202 showed similar overdominant effects (**Fig. 5**). In both *NILog* and *qILrg* heterozygotes had
203 significantly larger petals than homozygotes (effect sizes of 0.342 and 0.186 mm^2; SE = 0.132
204 and 0.0871; df = 19 and 20; t = 2.582 and 2.136; Bonferroni-adjusted p = 0.0183 and 0.0452,
205 respectively). Similarly, in complementation crosses, *Cg/crjag* heterozygotes produced larger
206 petals than *Cg/Cr* heterozygotes (**Fig. 2**). *JAG*, therefore, appears to be prone to overdominant
207 mutations, likely due to dosage-sensitive responses in petal development.

208 Such overdominance, if maintained by selection, could promote allele reuse by keeping
209 functionally divergent variants in the outcrosser population. To test this, we examined allele
210 frequencies across natural populations at polymorphic sites segregating between the haplotypes
211 used in transgenic assays (*Cg1- Cr* and *Cg2 - Co*). Of 642 polymorphic sites, 84 converged
212 between selfers. Yet, none of these sites were fixed, as selfer alleles still occurred at ≥4% in
213 *Cg*. This lack of strong differentiation excludes a scenario of parallel evolution via identical
214 independent changes at the same locus post-divergence. Both selfers also carried species-
215 specific alleles (16 in *Cr*, 26 in *Co*), indicating that independent de novo changes may also have
216 contributed (**Fig. S11**). Because the high number of convergent polymorphisms suggested
217 evolution via standing genetic variation, we tested whether selfer/outcrosser polymorphisms
218 segregating in *Cg* were associated with petal size (**Fig. 5 and S12**). Among 233 polymorphisms
219 with sufficient genotype counts, 15 were significantly correlated with petal length (FDR-

adjusted P < 0.05). Of these, nine showed overdominance, with heterozygotes having larger petals. Six of these nine were fixed in both selfers, and five were associated with smaller petals (**Fig. S12**). This suggests that collateral evolution through the fixation of multiple small-effect variants could also contributed to petal size reduction.

Because *Cg/Cr* and *Co* lineages diverged approximately 1 Mya, this scenario implies that these polymorphisms have persisted for thousands of generations (**Fig. 1**, (*48*, *49*)). Such persistence could plausibly be explained by heterozygote advantage, given the importance of petal size for pollinator attraction. However, none of the convergent overdominant polymorphisms showed significant deviations from Hardy-Weinberg equilibrium -(HWE) or evidence of heterozygote excess in *Cg* (**Fig. S13**). Nonetheless, in a population with a large effective population size, such as *Cg* (*50*), weak overdominant selection could maintain allele frequencies near a stable equilibrium without causing apparent departure from HWE (*51*). To test this hypothesis, we estimated selection coefficients acting on petal morphology by correlating petal size with reproductive efficiency in a hybrid outcrossing population (**Fig. S13B**). Using these estimates, together with the observed heterozygote effects, we modelled allele trajectories for each convergent overdominant polymorphism (**Fig. S13C**). Despite low selection coefficients (average s against homozygotes ≈ 0.0056), overdominant selection was sufficient to maintain these polymorphisms over millions of generations (probability of heterozygote maintenance: 1 with selection and drift vs. 0.18 under drift alone) (**Fig. S13C**). Consistent with our above analysis, only rare simulations (<0.05%) led to HWE departures. Together, these results indicate that weak overdominant selection can maintain functionally divergent alleles at polymorphic frequencies in large outcrossing populations, thereby enabling repeated recruitment of standing variation and facilitating phenotypic convergence through collateral evolution.

Implications for convergent evolution of selfing lineages

Petal reduction in both *Capsella* selfers arose through the identical developmental mechanism and the co-option of the same genetic solution (**Fig. S14**). In both lineages, cis-regulatory changes reduce the activity of *JAG*, a general growth promoter, leading to decreased cell proliferation in the distal petal margin. Although reduced *JAG* expression is detectable in several organs, only petals are strongly affected, likely because petal growth is more sensitive to *JAG* dosage. This heightened sensitivity appears to impose a developmental constraint on evolution by enabling large morphological changes in petals while limiting pleiotropic effects,

252 explaining at least in part gene reuse and the convergent evolution observed between
253 independent transitions to self-fertilisation. In addition, the reuse of standing variation also
254 appears to have facilitated phenotypic parallelism. Variants segregating at intermediate
255 frequency in *Cg*, where they influence petal size, have been similarly fixed in both selfing
256 lineages. Weak overdominant selection associated with improved pollinator attraction explains
257 the long-term persistence of these variants in *Cg,* and thus their repeated use. Together, our
258 findings illustrate how the interplay between standing genetic variation and developmental
259 constraints interact to bias evolutionary trajectory toward repeatable outcomes.

260

261 # Materials and methods

262 **Plant material**

263 This study used *Capsella rubella*, *C. orientalis*, and *C. grandiflora* accessions previously
264 described by (*37*). Near-isogenic lines (NILs) segregating for PAQTL_2 were generated by
265 introgressing the *Cg926* allele into *Cr1504* (*NILrg*) and *Co1983* (*NILgo*) through five and three
266 rounds of backcrossing, respectively, followed by two additional generations of selfing while
267 maintaining heterozygosity at the PAQTL_2 locus. Progeny from these two NILs were used for
268 fine mapping. The crossing scheme used to generate the quasi-isogenic line (qILrg) is shown
269 in **Fig. S4C**.

270 The *jag-2* EMS mutant in *Landsberg-erecta* (L-*er*) background showing recessive floral
271 phenotype was previously identified to have a single nucleotide change (C/T) in the second
272 exon resulting in a premature stop codon (*40*). Here, we have identified the *Crjag* mutant in *C.*
273 *rubella Cr22.5* background by screening a *C. rubella* (*Cr22.5*) ethyl-methanesulfonate (EMS)
274 mutagenized population for plants with reduced petal size (*52*). The genetic basis and
275 phenotypic characterization of this mutant are presented in this manuscript.

276 **Growth conditions**

277 Seeds were surface-sterilized, plated on half-strength Murashige-Skoog medium supplemented
278 with gibberellic acid (Duchefa Biochemie; 3.3 mg/L GA), and vernalized for two days at 4°C.
279 Germination occurred at 22°C for ten days. To initiate the transition to flowering, seedlings
280 were placed at 4°C for ten days. Subsequently, plants were grown in a growth chamber under

281 long-day conditions (16 hours light/8 hours dark) with a temperature cycle of 22°C during the
282 day and 16°C at night, 70% humidity, and a light intensity of 150 μmol $m^{-2}s^{-1}$.

283 **Morphological measurements**

284 To characterize the effect of PAQTL_2, diverse genetic constructs, and *jag* mutations, sizes of
285 the various organs were measured. Sepals, petals and anthers were measured from the 15th and
286 16th fully opened flowers on the main stem. Carpel length was measured from unfertilized
287 flowers. Six petals, six sepals, six anthers and two carpels were measured per plant. Dissected
288 flower organs were flattened and scanned at a resolution of 3200 dpi (HP ScanJet 4370).
289 Measurements were conducted on digitized images by using ImageJ (*53*). Leaf size was
290 measured on the fully expanded 6th leaf. The leaves were flattened and scanned at a resolution
291 of 300 dpi using an HP ScanJet 4370. Measurements were then taken from the digitized images
292 using ImageJ. (*53*).

293 **Morphometric analysis of petal outlines**

294 Morphometric analysis of petal shape described as closed outlines was performed using Elliptic
295 Fourier Descriptors (EFD) (*54*). First, the digital images were converted into binary images
296 using ImageJ (*53*). Coordinates of boundaries were extracted using the Python module scikit-
297 image (*55*). Outline coordinates were then analysed and visualised using the Momocs package
298 implemented in R (*56*).

299 **Developmental analysis of petal growth**

300 Petal cell size and cell number were determined from dried-gel agarose prints (*57*) of whole
301 petals from fully open flowers. Cell outlines were captured using and Olympus BX 51 light
302 microscope and AxioCam HRc camera (Carl Zeiss). The cell-outline images were merged using
303 the photomerge function of Adobe Photoshop and further processed with the Python module
304 scikit-image. First, cell-outlines were segmented using adaptive thresholding. Then, binary
305 images of cell borders were dilated, skeletonized and curated by overlapping them with the
306 original images in GIMP (https://www.gimp.org/). Cell areas and centroid coordinates were
307 extracted and used to estimate the average cell number and area per segment along the petal
308 longitudinal axis. The analysis of differences in cell number and size between genotypes was
309 performed using R (*58*). Curated segmented images were then analysed with ImageJ by defining

310 Region Of Interest (ROI) and measuring diverse morphological features for each particle.
311 Heatmap were generate in imageJ using ROI color coder function.

312 **Confocal imaging**

313 To visualize petal primordia, young flower buds were fixed in a solution containing 50%
314 methanol and 10% acetic acid. mPS-PI staining was carried out following the protocol by
315 Ichihashi et al. (2011)(*59*), with minor modifications. Imaging was performed using a confocal
316 laser scanning microscope (LSM780, Carl Zeiss), with excitation at 488 nm and emission
317 collected between 520 nm and 720 nm. Z-stack images were acquired at a resolution of 512 ×
318 512 with a step size of 0.5–1 µm along the z-axis. Image stacks were processed and analyzed
319 using MorphoGraphX (*60*, *61*). Surfaces were detected using the "edge detect" tool with a
320 threshold of 10,000. Initial meshes were generated with 5 µm cubes and subsequently
321 subdivided three times before projecting the mPS-PI signal located 4-6 µm from the mesh
322 surface.

323 **EDU staining**

324 Cell division events were visualized using a combination of 5-ethynyl-2'-deoxyuridine (EdU)
325 incorporation and modified pseudo-Schiff propidium iodide (PI; Sigma-Aldrich) staining,
326 following the protocol described in Riglet et al. (2024) with minor modifications (*62*).
327 Inflorescences were harvested and placed on EdU staining medium consisting of 0.22% (w/v)
328 Murashige and Skoog basal salts with vitamins (Duchefa Biochemie, M0222.0050), 3.5% (w/v)
329 sucrose, 0.8% (w/v) agarose, and 10 µM EdU (Invitrogen A10044, Thermo Fisher Scientific),
330 adjusted to pH 5.7. Samples were submerged in the same medium lacking agarose and
331 incubated for 15 hours in a growth chamber under long-day conditions (16-hour light/8-hour
332 dark photoperiod) at 22°C, with an average light intensity of 150 µmol $m^{-2}s^{-1}$. Following
333 incubation, samples were dehydrated through a graded ethanol series (25%, 50%, 75%, 90%,
334 and 100%; 10 minutes each), then rehydrated through the same series in reverse. Tissues were
335 then treated overnight at 37°C with 20 mM α-amylase (Sigma-Aldrich A4551) in phosphate
336 buffer (pH 7.0) supplemented with 2 mM NaCl and 0.25 mM $CaCl_2$. After washing twice with
337 water and once with 100 mM Tris buffer (pH 8), the samples were incubated for 1 hour in a
338 solution containing 10 µM Alexa Fluor 488-azide (Invitrogen A10266) in 100 mM Tris buffer
339 (pH 8). Subsequently, tissues were incubated for 30 minutes in a click-reaction solution
340 containing 10 µM Alexa Fluor 488-azide, 100 mM Tris (pH 8), 1 mM $CuSO_4$, and 100 mM
341 ascorbic acid. Samples were washed three times with water. Young flower buds were dissected

342 in water to expose petals and incubated in 1% periodic acid for 30 minutes, followed by two
343 water washes. Samples were then stained with 0.01 μg μl^{-1} PI for 3 hours, cleared for 2 hours
344 in chloral hydrate solution, and mounted in Hoyer's solution (30 g gum arabic, 200 g chloral
345 hydrate, 20 g glycerol, and 50 ml water). Imaging was performed using a confocal laser
346 scanning microscope (LSM780, Carl Zeiss) with excitation at 488 nm. Emission was collected
347 between 493–547 nm for EdU and 622–718 nm for PI. Z-stack images were acquired at 512 ×
348 512 resolution with a step size of 0.5–1 μm along the z-axis. EdU signals were detected and
349 quantified using ImageJ.

350 **Genetic mapping**

351 To refine the position of PAQTL_2, we conducted a segregation analysis in the *NILrg*
352 background. Initial mapping using approximately 400 progeny plants identified a 138.095 kb
353 region on chromosome 2, located between markers Bs5 (position 8,964,289) and SH3_2
354 (position 9,102,384) (**Table S3**). To further narrow down this interval, we screened about 1,000
355 additional progeny plants from NILrg to identify individuals with recombinant chromosomes
356 between these two markers. The positions of the recombination breakpoints were determined
357 by genotyping these recombinants with additional markers within the interval. Selfed progenies
358 from the 15 most informative recombinant lines were then genotyped to identify individuals
359 homozygous for either parental allele. Petal size was quantified in these homozygous plants,
360 and a t-test was used to compare the average petal size between genotype classes for each
361 recombinant to localize the causal mutation in relation to the position of each recombination
362 breakpoint.

363 For fine-mapping PAQTL_2 in the *NILgo* background, we first identified a *NILgo* line
364 segregating for a ~1 Mb region surrounding PAQTL_2, located between markers JAGI
365 (position 8,127,464) and m400 (position 9,149,587) on chromosome 2 (**Table S4**).
366 Approximately 1,400 NILgo progeny plants were screened to identify recombinants between
367 these markers. Each recombinant was genotyped with additional markers within the focal
368 region to pinpoint the recombination breakpoints. Selected recombinant plants were selfed, and
369 progeny were genotyped to identify individuals homozygous for either the *C. grandiflora* or *C.*
370 *orientalis* allele in the segregating region. As described above, petal sizes of both genotype
371 classes were measured and compared using a t-test, enabling us to further refine the position of
372 the causal mutation.

373 **Molecular cloning and plant transformation**

374 *C. rubella* (*JAGr*), *C. orientalis* (*JAGo*), two *C. grandiflora* (*JAGg1* and *JAGg2*) and two
375 promoter swap genomic constructs: *pJAGg1::JAGr* and *pJAGr::JAGg1* were used to test the
376 existence of allelic variation influencing petal size within the *JAG* locus. The 8.3 kb *JAGr*, 9.4
377 kb *JAGg*, 9.4 kb *pJAGg::JAGr* and 8.3kb *pJAGr::JAGg1* genomic constructs were amplified
378 in two PCR reactions from genomic DNA of plants homozygous for the *C. rubella* allele
379 (*NILrr)* and plants homozygous for the *C. grandiflora* allele (*NILgg1)* as described in **Table**
380 **S5**. The 8.3 kb *JAGo* and a 10.1 kb *JAGg2* genomic constructs were amplified in three PCR
381 reactions from genomic DNA of plants homozygous for the *C. orientalis* allele (*NILoo)* and
382 plants homozygous for the *C. grandiflora* allele (*NILgg2)* as described in **Table S5**. Primers
383 used are presented in **Table S6**. The genomic fragments were first assembled and subcloned
384 into a modified version of pBluescript II KS (StrataGene, pBlueMLAPUCAP) using the
385 InFusion® HD Cloning Plus kit (Clontech) and sequenced. The reconstituted cassettes were
386 transferred into the AscI site of the plant transformation vector pBarMAP, a derivative of
387 pGPTVBAR (*63*). These genomic constructs were then used to transform *Crjag* and *jag-2*
388 plants by floral dip (*64*). Note that since *NILrg* and *NILog* were generated from crosses with
389 different *Cg926* individuals and since *C. grandiflora* is a highly heterozygous outcrosser, the
390 two *C. grandiflora* allele were not identical in sequence and were therefore named *JAGg1* and
391 *JAGg2*.

392 **Identification of the *Crjag* mutation**

393 To identify the *Crjag* mutation, we followed a mapping-by-sequencing approach (*65*). 500 F2
394 progeny of a cross between a mutant that we initially termed *heart-stopping (hts)* because of
395 the defect in fruit development and *Cr1504* were screened to isolate plants with a WT or mutant
396 phenotype. About 100 plants for each genotype were pooled and sequenced using the Illumina
397 NextSeq 500 instruments (2 x 100 cycles). DNA-seq data were processed using Trimmomatic
398 (*66*) to remove adapter sequences. Quality control was done using FastQC
399 (http://www.bioinformatics.bbsrc.ac.uk/projects/fastqc). Reads were then mapped at per
400 sample level against the *C.rubella* reference genome (Cru_183 from phytozome.org) using
401 BWA-MEM (*67*). Variant calling was performed using SAMtools (*68*). Those calls were then
402 further processed using R (*58*) to extract *Cr22.5* (background of *crjag* mutation)/*Cr1504*
403 polymorphisms. The ratio between the number of homozygous and heterozygous calls within
404 200 kb windows was used to localize the mutation.

405 **RNA splicing analysis**

406 To detect splicing differences, RNA was first extracted from *Crjag* and *Cr22.5* inflorescences
407 (containing the inflorescence meristem and the flower buds from stage 1 to 9) using Trizol (Life
408 Technologies). RNAs were treated with TurboDNAse (Ambion) and reverse transcribed using
409 oligo(dT) and the Superscript III Reverse Transcriptase (Invitrogen). Primers onw545 and
410 onw546 were used to amplify full-length *JAG* transcripts.

411 **Modelling of petal growth**

412 The *Capsella* petal growth model is based on a 2D Arabidopsis thaliana petal growth model
413 developed by Susanna Sauret-Güeto *et al.*, 2013 (*44*). Models were specified and manipulated
414 using the MATLAB-based application *GFTbox* (*69*). Growth patterns are guided by spatially
415 distributed factors across a tissue framework, referred to as the canvas. In this model, the initial
416 canvas consists of approximately 2,300 elements and measures 30 µm in both width and length.
417 Each factor is assigned a value at either the segments or vertices of the canvas, where it
418 promotes growth rates through a linear function (**Fig. S8**).The model integrates two
419 interconnected regulatory networks:

420 - The Polarity Regulatory Network (PRN), which defines tissue polarity and orients
421 growth along the canvas.
422 - The Growth Rate Regulatory Network (GRRN), which modulates the local growth
423 rates.

424 Polarity is established by the propagation of the factor POL, from a proximal organizer
425 (PROXORG) toward a distal organizer called DISTORG. In the most realistic divergent model,
426 DISTORG is expressed at the distal petal margin where it consumes POL, creating a divergence
427 in the polarity field. This causes the growth direction to shift away from the petal midline and
428 toward the margins in the distal region. Another key factor, DISGRAD, is predominantly
429 expressed in the distal region, where it promotes growth perpendicular to the mid-petal axis
430 (Kpar, or Kper). This model successfully replicates *Arabidopsis thaliana* petal development
431 and is supported by molecular data, which, in accordance with our observations, suggest that
432 *JAG* functions as a distal factor DGRAD and that auxin biosynthesis and signaling are involved
433 in the establishment of the polarity field. Although this model accurately simulates *A. thaliana*
434 petal growth, it fails to reproduce the petal shape of *Capsella* species, despite very similar
435 overall growth rates (**Fig. S9**). In *C. grandiflora*, petal growth dynamics are similar to those of
436 *A. thaliana*, but the length-to-width ratio is significantly lower. Simply increasing Kper with

437 the basic growth parameter did not generate realistic *Cg* petal shapes, as it only widened the
438 distal region, maintaining a lobed shape, whereas *Cg* petals are generally more rounded. More
439 realistic outlines were obtained by expanding both the DISTORG and DGRAD domains.

440 However, reducing DGRAD activity in this modified model did not significantly decrease petal
441 length, as observed in *crjag* mutants (**Fig. 3**). To address this discrepancy, we modified the
442 model so that DGRAD also affected Kpar, which resulted in petals highly similar in shape and
443 size to those of *Cg*. Furthermore, abolishing DGRAD activity while accounting for the
444 fragmented distal auxin distribution in *jag* petals (as in (*44*)) led to a significant decrease in
445 petal length, resulting in 'jagged' petals approximately 1.5 mm long, closely resembling *crjag*
446 mutants. The models are provided as supplemental dataset and the parameters of the models
447 used are presented in **Table S7**.

448 Leaf growth was modeled using the organizer-based fixed polarity model described by Kuchen
449 et al. (2012) (*45*). In this model, tissue polarity is established by diffusion of a polarity factor
450 (POL) from a proximal organiser (PROXORG) at the base of the canvas. After an initial
451 equilibration phase, the POL gradient is fixed and deforms passively with the tissue during
452 growth. Growth parallel to the polarity field is promoted by PGRAD, while LAM promotes
453 growth perpendicular to the polarity. MID inhibits perpendicular growth along the midline, and
454 LATE modulates both parallel and perpendicular growth. All growth regulators remain fixed
455 to their initial spatial distributions throughout development.

456 **Population genetics**

457 We focused our analysis on polymorphisms segregating between the genotypes used for
458 transgenic analysis, as these carry the alleles responsible for variation in petal size between
459 mating strategies. Multiple sequence alignment of the four accessions (*C. rubella*, *C.*
460 *grandiflora Cg1* and *Cg2*, and *C. orientalis*) was performed using MAFFT. Polymorphisms
461 were identified from this alignment, which was then used to generate a consensus JAG sequence
462 including all indels and the most frequent alleles, using EMBOSS cons (parameters: -setcase 0
463 -plurality 1). This consensus sequence replaced the native *JAG* sequence in the *C. rubella*
464 reference genome (version 183).

465 We used this custom reference for read mapping of publicly available resequencing datasets
466 (GATK pipeline), including 180 *C. grandiflora* individuals from a single population, 51 *C.*
467 *rubella*, and 16 *C. orientalis* (*70–72*) (3 REFs). The resulting VCF file contained 3,300

468 polymorphisms in the *JAG* coding and cis-regulatory regions. Indels were normalized using
469 bcftools (norm followed by filter --IndelGap 5), applying parsimony and left-alignment, which
470 reduced the set to 2,371 polymorphisms. We further processed the VCF in R with custom
471 scripts, applying the following rules: (i) remove polymorphisms absent from the genotypes used
472 for introgression and complementation; (ii) simplify indel annotations not fully resolved during
473 normalization; and (iii) inspect ambiguous sites using IGV to resolve missing information.
474 After filtering, the final dataset contained 340 polymorphisms for the Cg-Cr comparison and
475 536 for the Cg–Co comparison. Among the 164 shared polymorphisms, i.e. the major allele in
476 Cg differs from the major allele of *Cr* and *Co*, 84 were called convergent, i.e. the fixed allele in
477 Cg (frequency >75%) differs from the fixed allele in Cr and Co (frequency >90%).
478 Polymorphism were considered to converge between selfer lineage when the same allele was
479 present at a frequency > 90% in the two selfers while remaining under 75% in the outcrosser.

480 To facilitate downstream association analyses, multiallelic sites in the VCF were decomposed
481 into biallelic pseudo-loci. For each multiallelic site, the list of alternative alleles was extracted,
482 and each ALT allele was treated as a separate locus. Genotypes were recoded as allele counts
483 (0, 1, or 2 copies of the ALT allele), with missing data set to NA. This procedure was applied
484 to all variants, and the resulting expanded genotype matrix was use for dowstream analysis.

485 **Phenotypic association analysis and detection of overdominance**

486 Phenotypic measurements for *Cg* individuals with available genomic information were retrieve
487 from (*26*) and filtered to remove individuals with missing values. Genotypic data were
488 converted into an individual-by-locus matrix, coded numerically, and merged with the
489 phenotypic dataset. For each trait–locus combination, we tested for overall genotype effects
490 using linear models with genotype as a categorical predictor. Loci with fewer than 10
491 individuals in any genotype class were excluded from analysis. The overall significance of
492 genotype effects was assessed by ANOVA, and per-term p-values were adjusted for multiple
493 testing using the Benjamini–Hochberg false discovery rate (FDR) procedure.

494 To formally test for overdominance, we applied an additive–dominance model in which
495 heterozygotes were explicitly coded as a binary variable. For each locus–trait pair with adequate
496 sample size in all three genotype classes, we fitted the model Phenotype ~ additive + dominance
497 and identified significant dominance effects ($p < 0.05$) where heterozygotes exceeded both
498 homozygotes in mean phenotype. Overdominant candidates were defined as loci that (i) showed
499 a significant dominance term, and (ii) had heterozygous mean phenotypes greater than both

homozygotes in the filtered dataset. Overlap between these statistical and phenotypic criteria was used to generate the final list of overdominant loci. Candidate loci were annotated with SNP metadata and visualized using boxplots and Manhattan-like genome position plots, with overdominant loci highlighted. The list of phenotype based overdominant polymorphisms was compared to the list of comvergent polymorphisms.

Identification of overdominant loci through inbreeding coefficient

Observed genotype counts per locus (*n*AA, *n*AB, *n*BB) were calculated from the expanded genotype matrix. From these, observed heterozygosity (H_o), expected heterozygosity (H_e), and the inbreeding coefficient ($F_{IS} = 1 - H_o/H_e$) were computed. Hardy–Weinberg equilibrium (HWE) exact tests were performed using the HardyWeinberg package in R. Loci were classified as overdominant if they satisfied all of the following criteria: (i) significant deviation from HWE ($p < 0.05$), (ii) negative F_{IS} values (heterozygote excess), and (iii) $H_o > H_e$. Chromosome-wise plots of F_{IS} against genomic position were generated marking overdominant loci and convergent overdominant (based on phenotype) candidates.

Simluation of the influence of overdominat selection on allele trajectories

We conducted a common garden experiment at the University of Potsdam, Germany, using an F_2 population derived from a cross between *Cg* and *Cr*. Plants homozygous for the Cg (functional) allele at the self-incompatibility locus were selected, and their petal size was quantified. Reproductive efficiency was estimated as the number of seeds produced per fruit (which reflect animal pollination), normalized by the average number of ovules developed by each individual.

The relationship between petal size and reproductive efficiency was assessed using Pearson's correlation. A linear regression model was then fitted with reproductive efficiency as the response variable and petal area as the predictor. Regression coefficients and R^2 values were extracted to describe the strength and direction of the relationship. For visualization, scatterplots with fitted regression lines and annotated regression equations were generated.

Allele frequency dynamics were simulated using a discrete-generation Wright–Fisher model. The model incorporated: Effective population size N_e=500,000, 10^6 generations and an initial allele frequency p_0 =0.1 and Selection coefficients derived from genotype-phenotype relationships. For each replicate (500 replicates), genotype frequencies were adjusted according to selection coefficients, and the next generation was sampled multinomially to

account for genetic drift. Simulations were also conducted under neutrality (no selection) for comparison.

Fitness of genotypes was modeled linearly as a function of deviation from the mean phenotypic value:

$$wi = 1 + \beta(Gi - \bar{G})$$

where β is the selection coefficient relating phenotype to fitness, Gi is the genotype's phenotypic value, and $\bar{G}$ is the population mean. Overdominance was assessed by comparing heterozygote fitness to the two homozygotes. A stable internal equilibrium allele frequency $\hat{p}$ was estimated when overdominance was detected.

For each simulation replicate, we recorded allele frequencies across generations and at the final generation: homozygote and heterozygote counts, observed heterozygosity (*Ho*), expected heterozygosity (*He*), and *Fis*. Hardy–Weinberg equilibrium was tested using exact tests, and the proportion of replicates deviating from equilibrium at α=0.05 was reported.

Allele frequency trajectories were summarized as mean ± 95% confidence intervals across replicates. Final-generation allele frequencies were visualized as histograms, and probabilities of maintaining polymorphism were estimated as the proportion of replicates with 0 < heterozygote frequency < 1.

Statistical analyses

Statistical analyses were performed using R (version 4.2.1). Two-tailed Student's t-test assuming unequal variances was used for two-sample comparisons. For multiple comparison, we conducted a Tukey's HSD tests were performed using the R/agricolae package. Data visualization was done using the R/ggplot2 package or R/base. Box plots were generated using the ggplot2 package implemented in R software. In all boxplots, the middle lines represent the median, the lower and upper hinges correspond to the first and third quartile, respectively. The upper and lower whiskers add or subtract 1.5 interquartile ranges to/from the 75 and 25 percentile, respectively. Overdomiance was tested using Linear mixed-effects models were fitted using the lmer function in the lme4 package. Estimated marginal means were obtained using the emmeans package. Planned contrasts between genotypes were tested with Bonferroni-adjusted p-values, and degrees of freedom were approximated using the Kenward-Roger method.

References

1. D. L. Stern, *Nat. Rev. Genet.* **14**, 751–64 (2013).

2. Z. D. Blount, R. E. Lenski, J. B. Losos, *Science (80-.).* **362** (2018), doi:10.1126/science.aam5979.

3. T. D. Hether, P. A. Hohenlohe, *Evolution (N. Y).* **68**, 950–964 (2014).

4. Stephen Jay Gould, Wonderful Life: The Burgess Shale and the Nature of History (W.W. Norton & Company, 1989).

5. P. K. Hoitinga, S. Birkeland, *Trends Genet.* (2025), doi:10.1016/j.tig.2025.06.009.

6. T. Tsuchimatsu, S. Fujii, *Philos. Trans. R. Soc. B Biol. Sci.* **377** (2022), doi:10.1098/rstb.2020.0510.

7. K. K. Shimizu, T. Tsuchimatsu, *Annu. Rev. Ecol. Evol. Syst.* **46**, 112414–054249 (2015).

8. S. I. Wright, R. W. Ness, J. P. Foxe, S. C. H. Barrett, *Int. J. Plant Sci.* **169**, 105–118 (2008).

9. R. Cruden, *Biol. J. Linn. Soc.*, 32–46 (1977).

10. S. C. H. Barrett, *Nat. Rev. Genet.* **3**, 274–84 (2002).

11. A. Blarer, T. Keasar, A. Shmida, *Ethology* (2002), doi:10.1046/j.1439-0310.2002.00778.x.

12. C. B. Fenster, G. Cheely, M. R. Dudash, R. J. Reynolds, *Am. J. Bot.* (2006), doi:10.3732/ajb.93.12.1800.

13. C. Goodwillie *et al.*, *New Phytol.* **185**, 311–321 (2010).

14. A. Sicard, M. Lenhard, *Ann. Bot.* **107**, 1433–1443 (2011).

15. L. Fishman, A. J. Kelly, J. H. Willis, *Evolution (N. Y).* **56**, 2138–2155 (2002).

16. L. Fishman, P. M. Beardsley, A. Stathos, C. F. Williams, J. P. Hill, *New Phytol.* (2015), doi:10.1111/nph.13091.

17. J. Z. Lin, K. Ritland, *Genetics*. **146**, 1115–1121 (1997).

587 18. C. Goodwillie, C. Ritland, K. Ritland, *Evolution*. **60**, 491–504 (2006).

588 19. M. S. Georgiady, R. W. Whitkus, E. M. Lord, *Genetics*. **161**, 333–344 (2002).

589 20. M. A. Grillo *et al.*, *Evolution (N. Y).* (2009), doi:10.1111/j.1558-5646.2008.00602.x.

590 21. T. Slotte, K. M. Hazzouri, D. Stern, P. Andolfatto, S. I. Wright, *Evolution*. **66**, 1360–74
591 (2012).

592 22. A. Sicard *et al.*, *Plant Cell*. **23**, 3156–71 (2011).

593 23. A. Frary, L. A. Fritz, S. D. Tanksley, *Theor. Appl. Genet.* (2004), doi:10.1007/s00122-
594 004-1669-x.

595 24. D. L. Stern, V. Orgogozo, *Evolution*. **62**, 2155–77 (2008).

596 25. E. L. Dittmar, C. G. Oakley, J. K. Conner, B. A. Gould, D. W. Schemske, *Proc. R. Soc.*
597 *B Biol. Sci.* **283**, 20153065 (2016).

598 26. A. Sicard *et al.*, *Proc. Natl. Acad. Sci.* **113**, 13911–13916 (2016).

599 27. T. Slotte, K. M. Hazzouri, D. Stern, P. Andolfatto, S. I. Wright, *Evolution*. **66**, 1360–74
600 (2012).

601 28. T. Slotte *et al.*, *Nat. Genet.* **45**, 831–5 (2013).

602 29. F. Jantzen *et al.*, *New Phytol.* **224**, 1349–1360 (2019).

603 30. C. Sas *et al.*, 3313–3319 (2016).

604 31. N. J. Wozniak *et al.*, *Plant Cell*, in press, doi:10.1105/tpc.19.00551.

605 32. N. J. Woźniak *et al.*, *Curr. Biol.* **34**, 2702-2711.e6 (2024).

606 33. U. Fujikura *et al.*, *Dev. Cell*. **44**, 192-203.e5 (2017).

607 34. Y. Brandvain, T. Slotte, K. M. Hazzouri, S. I. Wright, G. Coop, *PLoS Genet.* **9**,
608 e1003754 (2013).

609 35. J. A. Bachmann *et al.*, *bioRxiv* (2018), doi:10.1101/425389.

610 36. H. Hurka, N. Friesen, D. A. German, A. Franzke, B. Neuffer, *Mol. Ecol.* (2012),
611 doi:10.1111/j.1365-294X.2012.05460.x.

37. A. Wozniak, N., Kappel, C., Marona, C. Altschmied, L., Neuffer B., Sicard, “Chapter 2 : A common molecular basis to the convergent evolution of the selfing syndrome in Capsella.”

38. N. J. Woźniak *et al.*, *Plant Cell*. **32**, 935–949 (2020).

39. A. Sicard *et al.*, *Plant Cell*. **23**, 3156–3171 (2011).

40. C. K. Ohno, *Development* (2004), doi:10.1242/dev.00991.

41. T. L. Turner, *Mol. Ecol.* **23**, 2377–2382 (2014).

42. S. Sauret-Güeto, K. Schiessl, A. Bangham, R. Sablowski, E. Coen, *PLoS Biol.* **11** (2013), doi:10.1371/journal.pbio.1001550.

43. K. Schiessl, J. M. Muiño, R. Sablowski, *Proc. Natl. Acad. Sci.* **111**, 2830–2835 (2014).

44. S. Sauret-Güeto, K. Schiessl, A. Bangham, R. Sablowski, E. Coen, *PLoS Biol.* **11**, e1001550 (2013).

45. E. E. Kuchen *et al.*, *Science (80-.).* **335**, 1092–1096 (2012).

46. J. R. Dinneny, *Development*. **131**, 1101–1110 (2004).

47. X. He *et al.*, *Cell Rep.* **44**, 115950 (2025).

48. H. Hurka, N. Friesen, D. a German, A. Franzke, B. Neuffer, *Mol. Ecol.* **21**, 1223–38 (2012).

49. J. A. Bachmann *et al.*, *New Phytol.* **224**, 505–517 (2019).

50. J. P. Foxe *et al.*, *Proc. Natl. Acad. Sci. U. S. A.* **106**, 5241–5 (2009).

51. J. Lachance, *Genet. Sel. Evol.* **41**, 15 (2009).

52. S. Streubel, M. A. Fritz, M. Teltow, C. Kappel, A. Sicard, *Development* (2018).

53. M. D. Abramoff, P. J. Magalhaes, S. J. Ram, *Biophotonics Int.* (2004), doi:DOI: 10.1016/S0022-3115(02)01073-5.

54. F. P. Kuhl, C. R. Giardina, *Comput. Graph. image Process.* **18**, 236–258 (1982).

55. S. van der Walt *et al.*, *PeerJ*. **2**, e453 (2014).

56. J. Claude, *Morphometrics with RNo Title* (Springer-Verlag New York, 2008).

637 57. G. Horiguchi, U. Fujikura, A. Ferjani, N. Ishikawa, H. Tsukaya, *Plant J.* **48**, 638–644
638 (2006).

639 58. R Core Team, R Found. Stat. Comput. Vienna, Austria. (2018).

640 59. Y. Ichihashi *et al.*, *Plant Physiol.* **157**, 1151–1162 (2011).

641 60. P. Barbier de Reuille *et al.*, *Elife*. **4**, 1–20 (2015).

642 61. S. Strauss *et al.*, *Elife*. **11** (2022), doi:10.7554/eLife.72601.

643 62. L. Riglet *et al.*, *Sci. Adv.* **10** (2024), doi:10.1126/sciadv.adp5574.

644 63. D. Becker, E. Kemper, J. Schell, R. Masterson, *Plant Mol. Biol.* **20**, 1195–1197 (1992).

645 64. S. J. Clough, A. F. Bent, *Plant J.* (1998), doi:10.1046/j.1365-313X.1998.00343.x.

646 65. G. V. James *et al.*, *Genome Biol.* (2013), doi:10.1186/gb-2013-14-6-r61.

647 66. A. M. Bolger, M. Lohse, B. Usadel, *Bioinformatics*. **30**, 2114–2120 (2014).

648 67. H. Li, *arXiv Prepr. arXiv*. **00**, 3 (2013).

649 68. H. Li *et al.*, *Bioinformatics*. **25**, 2078–9 (2009).

650 69. R. Kennaway, E. Coen, A. Green, A. Bangham, *PLoS Comput. Biol.* **7**, e1002071
651 (2011).

652 70. J. A. Agren *et al.*, *BMC Genomics*. **15**, 602 (2014).

653 71. D. Koenig *et al.*, *Elife*. **8**, 1–27 (2019).

654 72. E. B. Josephs, Y. W. Lee, J. R. Stinchcombe, S. I. Wright, *Proc. Natl. Acad. Sci. U. S.*
655 *A.* **112**, 15390–15395 (2015).

656

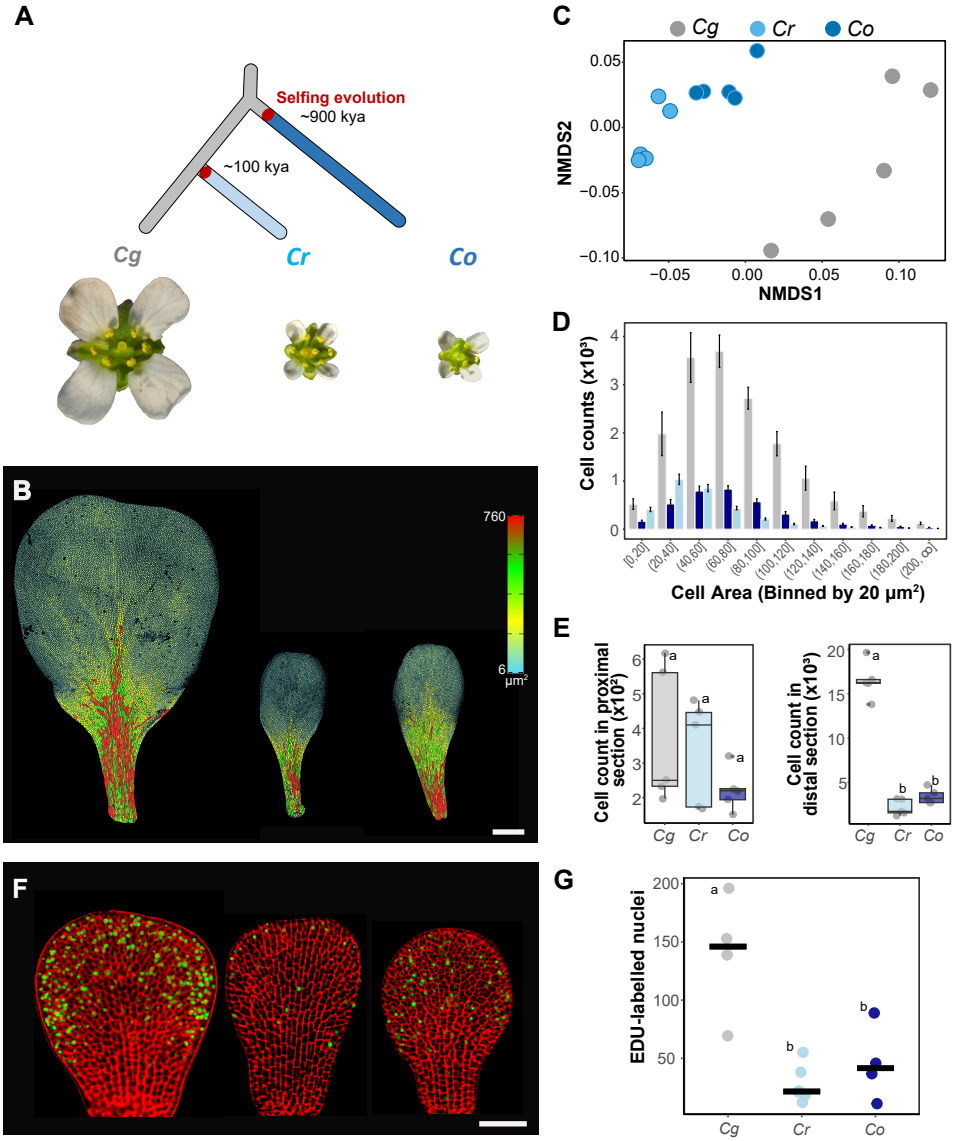

Figure 1: Convergent evolution of petal size following the transition to selfing in *Capsella*.

(**A**) Schematic representation of the evolutionary history within the *Capsella* genus. (**B**) Heatmap illustrating the distribution of cell size within the petals of the three *Capsella* species. Scale bar: 400 µm. (**C**) Non-metric multidimensional scaling (NMDS) plot based on Bray-Curtis dissimilarities in cellular features among *C. grandiflora*, *C. rubella*, and *C. orientalis* petals (n = 5 per species). (**D**) Average cell count per cell area bin (n = 5 per species). (**E**) Cell counts within the proximal and distal regions of the petals. (**F**) Representative images showing the distribution of cell division events across the epidermis of stage 1 petals. Fluorescently labeled nucleotide analog 5-ethynyl-2'-deoxyuridine (EdU; green) was used to visualize newly synthesized DNA, and primary cell walls were stained with propidium iodide (PI; red). Scale bar: 50 µm. (**G**) Quantification of EdU-labeled nuclei in stage 1 petals. Letters indicate significant differences as determined by one-way ANOVA with Tukey's HSD test (α = 0.05).

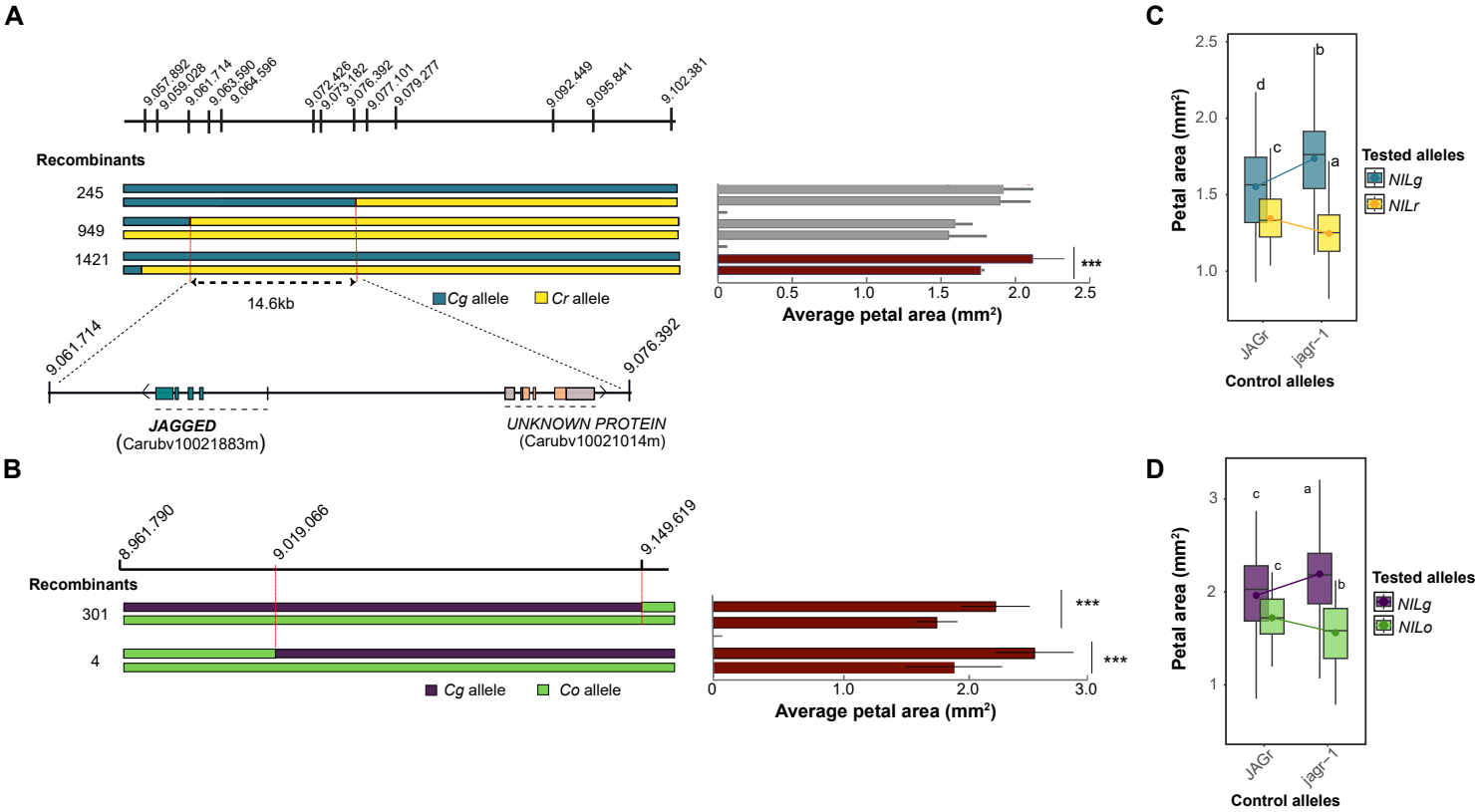

Figure 2: Allelic variation within JAG contribute to petal size reduction in indepdent selfing lineages.

(**A**) and (**B**) Fine mapping of PA_QTL2 in *C. rubella* (*Cr*) and *C.orientalis (Co)*, respectively.. The color coded bars on the left repsent the genotype of the most informative recombinants. The position on scaffold 2 are indicated on the top in base pair (bp). The bar chart on the rigth shows the average petal size for each alternative homozygous plants for each recombinant lines. Red filled bars indicates significant differences between alternative homozygous genotype P <0.05 (Student's t-test) (**C**) and (**D**) Quantitative complementation assay illustrated with an interaction plot of the crosses between *NILrg* (**C**) or *NILog* (**D**) with *jagr-1+/-*. Letters indicate significant differences as determined by one-way ANOVA with Tukey's HSD test (α = 0.05).

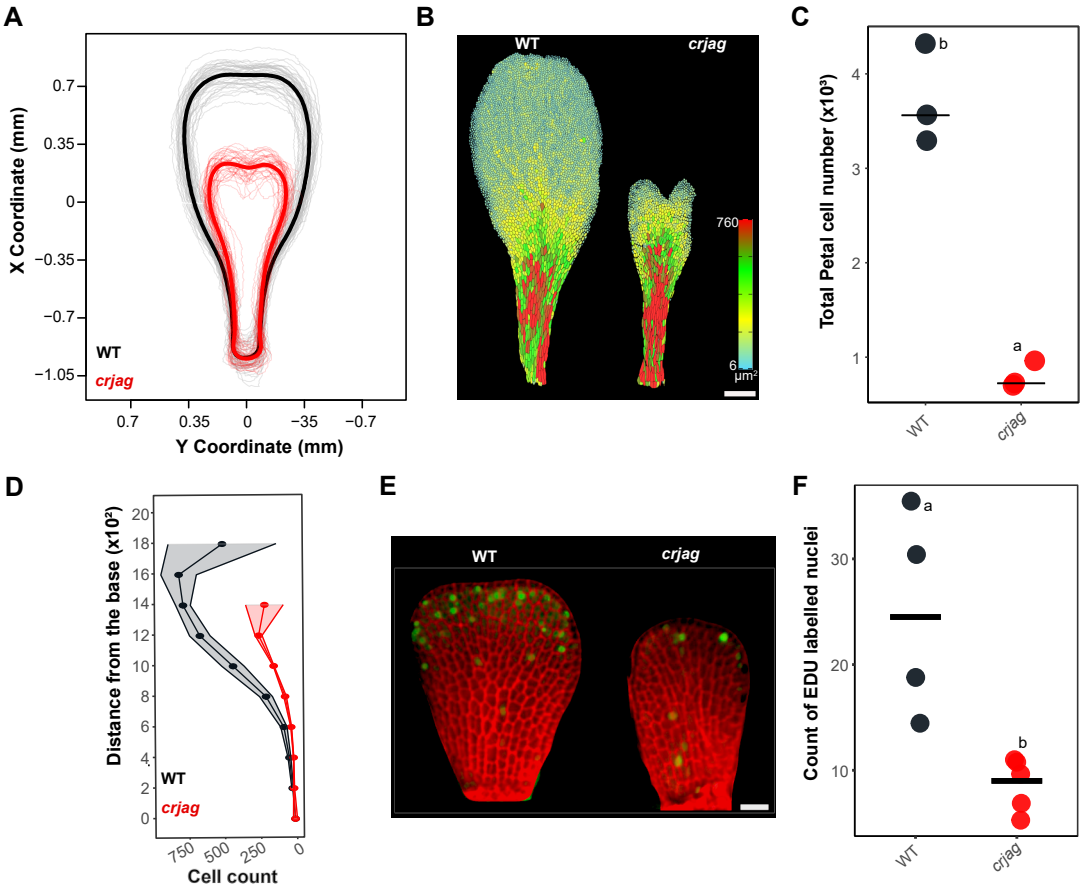

Figure 3: Loss of *JAG* function strongly inhibits cell proliferation during petal growth.

(**A**) Average shape of *Cr* and *crjag* petals. (**B**) Heatmap illustrating the distribution of cell size within the petals of *Cr* and *crjag*. Scale bar: 200 µm. (**C**) Total number of cell within *Cr* and *crjag* petals (n = 3 per genotype). (**D**) verage cell count per 200 µm section along the longitudinal petal axis (n = 3 per genotype). Numbers on the y-axis indicate the starting point of each section. (**E**) Representative images showing the distribution of cell division events across the epidermis of stage 1 petals. Fluorescently labeled nucleotide analog 5-ethynyl-2'-deoxyuridine (EdU; green) was used to visualize newly synthesized DNA, and primary cell walls were stained with propidium iodide (PI; red). Scale bar: 20 µm. (**F**) Quantification of EdU-labeled nuclei in stage 1 petals. Letters indicate significant differences as determined by one-way ANOVA with Tukey's HSD test (α = 0.05).

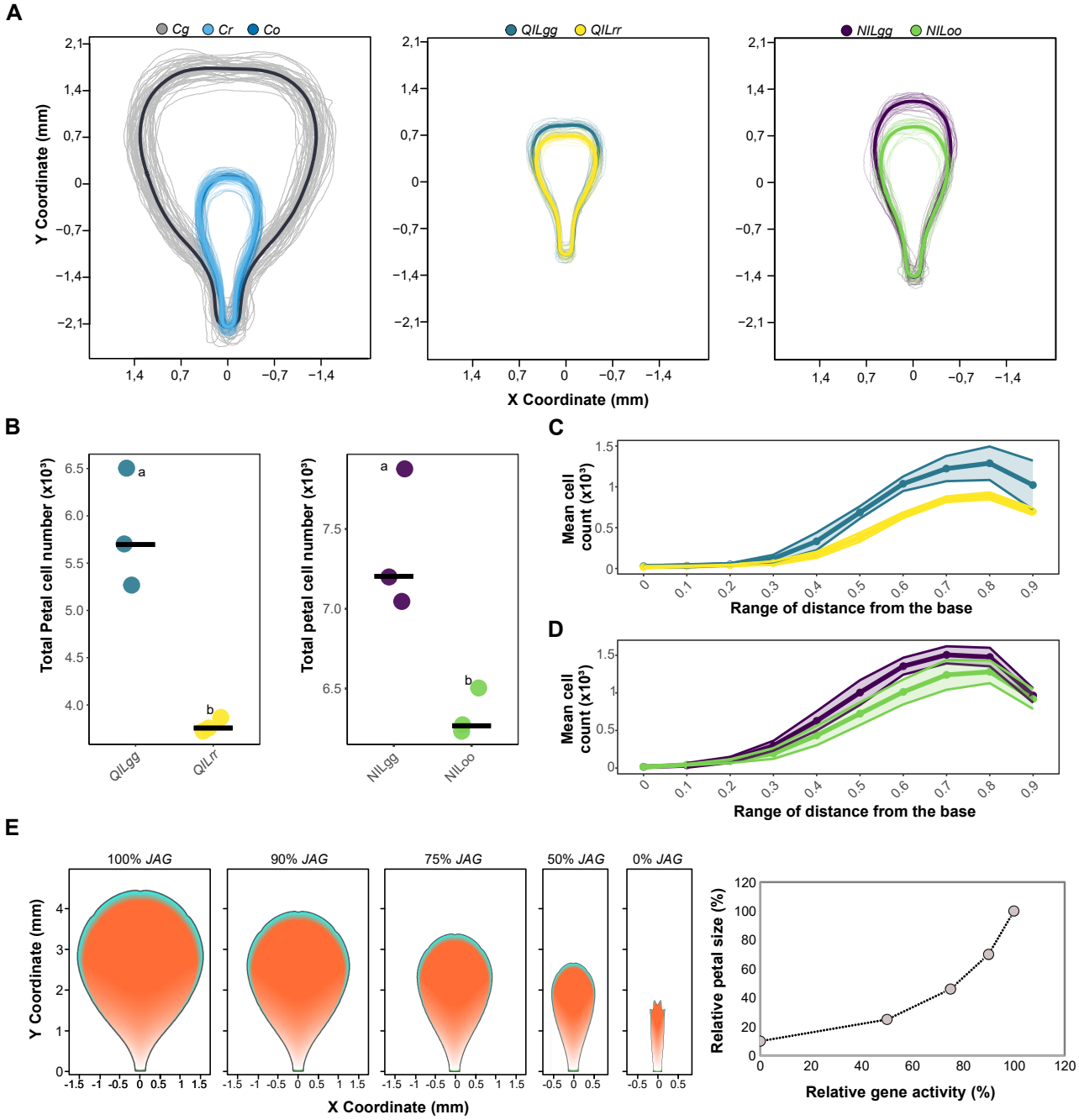

Figure 4: Developmental constraint on petal size evolution via heightened *JAG* sensitivity.

(**A**) Average petal shape of *Cg*, *Cr* and *Co* petals (left panel), of quasi Isogenic lines (*QIL*) homozygous for the *Cg1JAG* (QILgg) or *CrJAG* (QILrr) allele (middle panel) and of Near Isogenic lines (*QIL*) homozygous for the *Cg2JAG* (*NILLgg*) or *CoJAG* (*NILLoo*) allele (right panel). (**B**) Total number of cell within *QILgg* and *QILrr* and within *NILgg* and *NILoo* petals (n = 3 per genotype). (**C-D**) Average cell count for 10 section along the longitudinal axis within *QILgg* and *QILrr* (**C**) and within *NILgg* and *NILoo* (**D**) petals (n = 3 per genotype). Numbers on the y-axis indicate the starting point of each section. (**E**) Output of the Capsella petal development model with a divergent polarity field. The effect of *JAG* on basic growth parameters was progressively reduced, as indicated at the top of each graph from left to right. The rightmost graph shows the impact of decreased *JAG* activity on petal size. Letters indicate significant differences as determined by one-way ANOVA with Tukey's HSD test (α = 0.05).

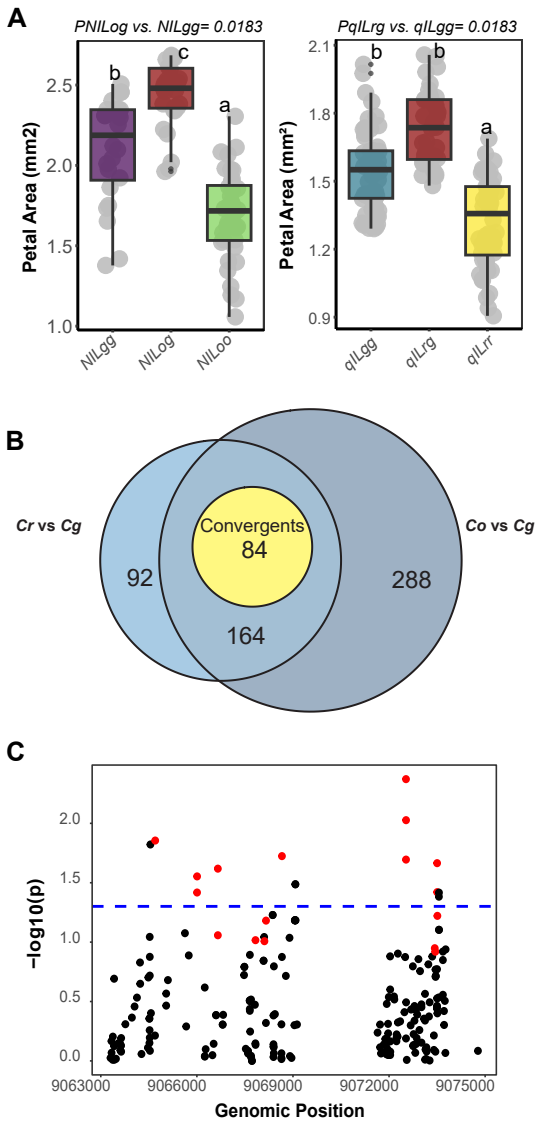

Figure 5: Standing genetic variation in *Cg* contribute to convergence.

(A) Relationship between petal size and JAG genotypes in the NILog and qILrg lines. Data points are gray dots; boxplots show petal area distribution per genotype. Letters denote significant differences from Tukey tests after a mixed-effects model with plant as a random effect. Bonferroni-adjusted p-values compare heterozygotes to larger homozygotes. (B) Venn diagram depicts lineage-specific and shared polymorphic sites between the two Capsella selfer lineages versus their outcrossor ancestor. Convergent polymorphism where the same allele was fixed in both of the selfers are highlighted in yellow (C) Manhattan like-plot displays genotype-phenotype (petal length) associations and overdominant loci. Each point tests a genomic locus' association with petal length; x-axis shows position; y-axis shows -log10(p), significance from linear model testing genotype effect on the phenotype. The dashed line marks p=0.05. Overdominant loci, where heterozygotes show the largest mean, are in red.